ENVIRONMENTAL STUDIES

The lunar nodal cycle controls mangrove canopy cover on the Australian continent

Neil Saintilan[1]*, Leo Lymburner[2], Li Wen[3], Ivan D. Haigh[4], Emma Ai[2], Jeffrey J. Kelleway[5], Kerrylee Rogers[5], Tien Dat Pham[1], Richard Lucas[6]

Long-phase (interannual) tidal cycles have been shown to influence coastal flooding and sedimentation, but their role in shaping the extent and condition of tidal wetlands has received little attention. Here, we show that the 18.61-year lunar nodal cycle, popularly termed the "lunar wobble," is a dominant control over the expansion and contraction of mangrove canopy cover over much of the Australian continent. Furthermore, the contrasting phasing of the 18.61-year lunar nodal cycle between diurnal and semidiurnal tidal settings has mediated the severity of drought impacts in northern bioregions. Long-phase tidal cycles regulate maximum tide heights, are an important control over mangrove canopy cover, and may influence mangrove ecosystem services including forest productivity and carbon sequestration at regional scales.

INTRODUCTION

Over interannual time scales, precessions in the orbit of the moon drive variability in tidal range principally over two time scales: the 18.61-year lunar nodal cycle and the 8.85-year cycle of lunar perigee, which influences high tide levels over a 4.4-year cycle (the lunar perigean subharmonic) (*1*). Interannual tidal cycles have previously been demonstrated to influence hydrodynamic energy, altering patterns of sedimentation (*2*, *3*), and coastal erosion (*4*), water level, and coastal flooding risk (*5*). To date, little, if any, consideration has been given to the influence of multiyear and decadal tidal cycles on the structure and function of tidal wetland ecosystems. Vegetated tidal wetlands (such as mangroves and tidal marsh) occur between mean sea level and mean high water spring tides (*6*), a position in the tidal frame likely to be strongly influenced by long period alterations in tidal range.

The influence of long-phase tidal harmonics on mangrove growth may be important over much of the Australian continent (Fig. 1). The influence of the 18.61-year nodal cycle on tidal amplitude is ~10 to 20 cm across much of the northern coastline, while a similar magnitude is evident for the 4.4-year perigean subharmonic on the Kimberly and Dampier coastlines in the West and the northern Great Barrier Reef coastline in the east (Fig. 1 and Materials and Methods) (*1*, *7*). In the Gulf of Carpentaria, the combined influence of the 18.61-year nodal cycle and the 4.4-year perigean subharmonic on the maximum tide height is ~30 to 40 cm, among the highest in the world (*1*). This variability in tidal amplitude is potentially higher than other influences on water level in upper intertidal environments, with the effect temporally clustered such that the influence is sustained over successive extremes of tidal amplitude minima and maxima (*5*).

Previous observations from northern Australia suggest the possible influence of long-phase tidal harmonics on coastal processes. Multidecadal phases of mangrove creek extension have been previously noted for the Kakadu region (*8*), the period of each wave of extension being ~two decades (*9*, *10*). The authors could not point to a hydrological driver of this change, noting that sea level trends for the period showed a slightly falling trend of 0.4 mm year^{-1} (*10*). The largest mangrove dieback event recorded globally, involving more than 1000 km of mangrove shoreline in the Gulf of Carpentaria (*11*) in 2015/2016, has been linked to a weakening of the monsoon wet season, lower than average rainfall, and a temporary decrease in mean sea level (*10*). These conditions were driven by an extreme negative phase of the El Niño Southern Oscillation (ENSO) coincident with a positive phase of the Indian Ocean Dipole (IOD) (*11*, *12*). However, dieback in the adjacent Arnhem and Great Barrier Reef bioregions was far less severe, despite the similar imposition of the ENSO and IOD events on sea level and climate.

Here, we test whether the 18.61-year nodal tidal cycle and the 4.4-year perigean subharmonic influence mangrove canopy expansion and contraction in Australia. Mangroves are pan-continental in distribution, reaching their greatest diversity and extent in the tropical north (*13*). They are absent from Tasmania and scarce in the arid southwest of the continent. Mangrove extent and cover for every year between 1987 and 2020 were quantified for the entire Australian continent using Landsat sensor data at 25-m resolution, nominally at a 16-day frequency (Materials and Methods) (*14*). The percentage of the Planimetric Canopy Cover (PCC%) was calculated for each calendar year, and the extent of canopy classes of closed forest (>80% cover), open forest (50 to 80% cover), and woodland (20 to 50% cover) was collated at the scale of coastal bioregions. Bioregions were grouped into those for which the 18.61-year tidal modulation was predicted to be important (Table 1), whether diurnal (the Gulf of Carpentaria; subdivided into three regions: group 1) or semidiurnal (Arnhem and Carnarvon bioregions: group 2) (Fig. 1). We also included four bioregions within which the 4.4-year modulation was predicted to influence maximum tidal variation (the Northern Great Barrier Reef, Bonaparte, Kimberley Coast, and Dampier Coast: group 3) and bioregions for which neither the 18.61-year nodal cycle nor the 4.4-year perigean subharmonic was modeled to be important [combined influence of less than ~6 cm; South East (SE) Queensland and SE Coast and Temperate Southern Coast: group 4], regions in which rainfall has previously been proposed as a control on mangrove extent and canopy cover (Table 1) (*15*–*17*).

We compared changes in the extent of mangrove cover and the proportion of closed forest canopy (an indicator of dieback if negative

[1]School of Natural Sciences, Macquarie University. [2]Department of Planning and Environment. [3]Department of Planning, Industry and Environment, Parramatta, NSW, Australia. [4]National Oceanography Centre, University of Southampton, Southampton, UK. [5]School of Earth, Atmospheric, and Life Sciences, University of Wollongong, Wollongong, NSW, Australia. [6]Aberystwyth University, Wales, UK. *Corresponding author. Email: neil.saintilan@mq.edu.au

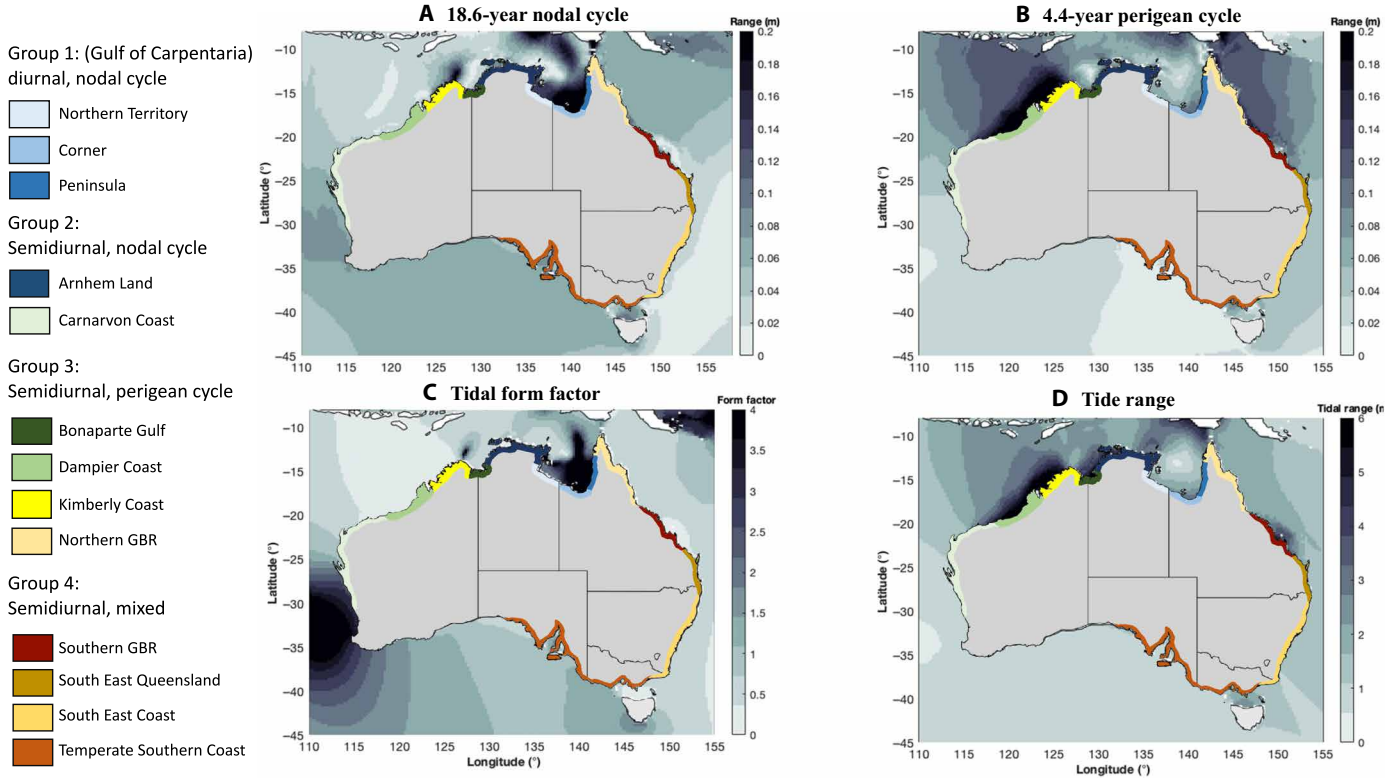

Fig. 1. Long-phase tidal cycles influencing Australian coastal bioregions. The modeled influence of the 18.6-year nodal cycle (**A**) and the 4.4-year perigean cycle (**B**) on tidal amplitude (Materials and Methods). Tidal form factor (**C**) ranges from semidiurnal (<0.25) to diurnal (>3), which influences the phasing of the nodal tidal cycle. Tidal range (**D**) varies markedly between bioregions.

Table 1. Tidal properties, rates of relative sea level rise, and mangrove area. Overall linear trend in monthly mean and maximum water level (mm year^{-1}) and the linear rate before and following the nodal diurnal tide maxima in 2006 (Gulf: Milner Bay; Kakadu: Darwin; Dampier, Kimberly, and Carnarvon: Broome; Northern Great Barrier Reef (Nth GBR): Cape Ferguson; Southern Great Barrier Reef (Sth GBR): Rosslyn Bay; Southern Queensland (Qld): Rosslyn Bay; Southeast (SE) Coast: Port Kembla; and Temperate Southern Coast: Portland) (Materials and Methods). Mangrove area in 2020 (woodland, open forest, and closed forest combined). SL, sea level.

Bioregion (group)	Tidal character (range, form, cycle)	Mean SL (1993–2020) (mm year^{-1})	Max SL (1993–2020) (mm year^{-1})	Max SL (1993–2006) (mm year^{-1})	Max SL (2007–2020) (mm year^{-1})	Mangrove (2020) (km^2)
Gulf (1)	Mesotidal, diurnal, 18.6 years	3.43	3.47	6.97	−25.29	646
Arnhem (2)	Mesotidal, semidiurnal, 18.6 years	4.71	5.00	−14.13	−0.02	3274
Carnarvon (2)	Mesotidal, semidiurnal*, 18.6 years	5.37	2.19	−14.12	6.17	378
Bonaparte (3)	Mesotidal, semidiurnal, 4.4 years	4.71	5.00	−14.13	−0.02	610
Kimberly (3)	Macrotidal, semidiurnal, 4.4 years	5.37	2.19	−14.12	6.17	1086
Dampier (3)	Macrotidal, semidiurnal, 4.4 years	5.37	2.19	−14.12	6.17	317
Nth GBR (3)	Mesotidal, semidiurnal, 4.4 years	4.53	5.84	0.11	−2.23	1620
Sth GBR (4)	Macrotidal, semidiurnal	4.78	6.75	−1.02	0.89	1013
SE Qld (4)	Mesotidal, semidiurnal	4.78	6.75	−1.02	0.89	418
SE Coast (4)	Mesotidal, semidiurnal	3.69	3.94	7.010	2.15	85.7
Temperate (4)	Mesotidal, semidiurnal	2.85	2.41	7.34	−9.86	207

*The diurnal component of the Carnarvon bioregion contains <2 km^2 mangrove.

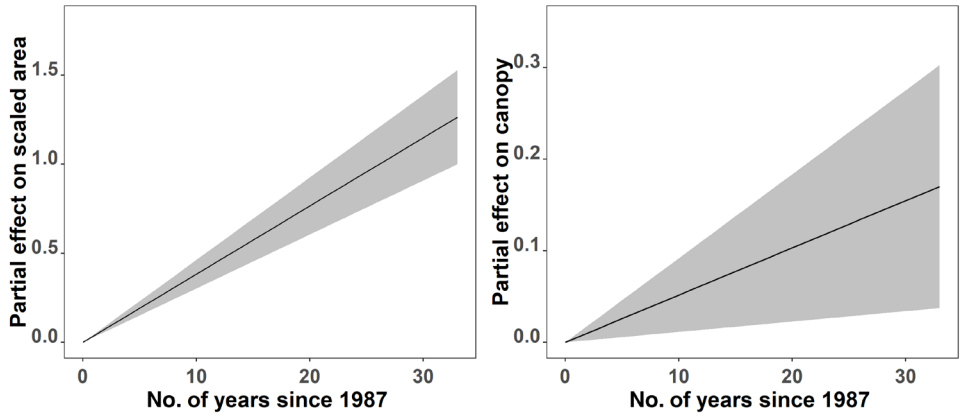

Fig. 2. Fitted overall trends of mangrove area and canopy condition (proportion of closed forest) Black lines are the estimate, and gray shaded areas are 95% confident intervals. Across the coastal bioregions, both the extent and canopy condition of mangrove increased significantly ($P < 0.001$ for both canopy condition model and area model; table S1). The partial effect is the effect of "year" on the dependent variable when the other independent variables are kept constant.

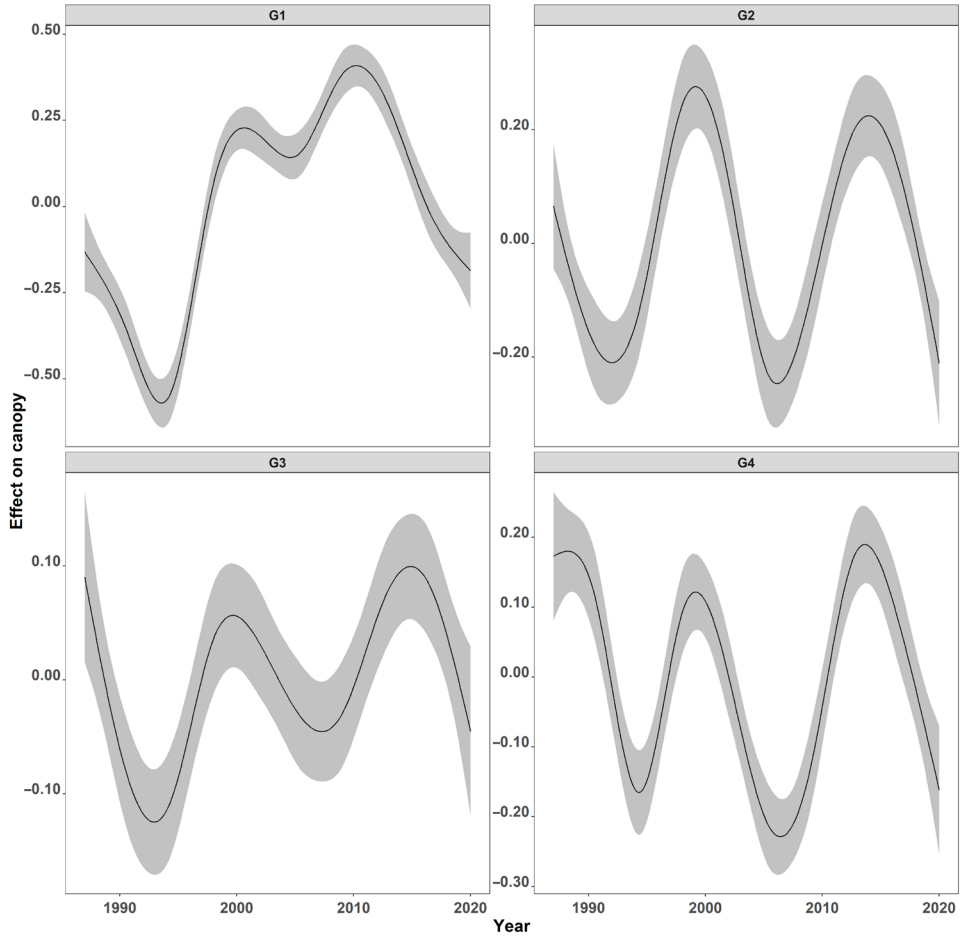

Fig. 3. Fitted long-term trends of mangrove canopy cover (proportion of closed forest to total mangrove area) at each bioregion after removing the overarching increasing trend. Black lines are the estimate, and gray shaded areas are 95% confident intervals. Note the differences in the *y*-axis scale. G1, Gulf; G2, Arnhem/Carnarvon; G3, Bonaparte/Kimberly/Dampier/Northern Great Barrier Reef; G4, Southern Great Barrier Reef/SE Queensland/SE Coast/Temperate as in Fig. 1 and Table 1.

and vegetative thickening if positive) with the lowest monthly maximum water levels, which occur during the dry season (August to November) due to prevailing easterly trade winds (*18*). We related interannual patterns in the lowest monthly maximum water level to the modeled influence of the 18.61-year lunar nodal cycle and the 4.4-year perigean subharmonic (Materials and Methods). Our hypothesis was that inundation high in the tidal frame (and consequently the duration of mangrove inundation within this period)

would be reduced under the low amplitude phase of the 18.61- and 4.4-year tidal cycles, leading to a reduction in hydroperiod, elevated water stress, and lower mangrove canopy cover.

These changes are expected to occur in the context of an overarching signal of climate change, associated with rising sea levels, higher air temperatures, and elevated atmospheric CO_2, all factors associated with mangrove expansion, increasing productivity, and canopy thickening (*6*). Statistical modeling was undertaken to decompose time series mangrove extent and proportion of closed canopy data within coastal bioregions into components describing the length of record trend and short-term fluctuations. Models were also developed for each coastal bioregion to investigate the response of mangroves to tidal and climatic variables.

RESULTS

Across all coastal bioregions, an overarching trend of increasing mangrove extent and canopy cover over time was established ($P < 0.0001$; Figs. 2 and 3 and table S1). Mangrove canopy cover was strongly related to the mean sea level, lowest maximum water level each year, and annual rainfall (bioregional group model r^2 ranging from 0.62 to 0.97; Fig. 4 and table S2), the relative importance of these factors varying between bioregion groupings as predicted by the strength of the nodal tidal cycle.

In the semidiurnal coastlines of the Carnarvon and Arnhem bioregions, patterns of closed canopy expansion and open forest and woodland contraction were synchronized (Figs. 5 and 6). In addition, phases of high canopy cover corresponded to high tidal amplitude phases of the 18.61-year lunar nodal cycle (Figs. 5 and 6). This pattern held over the two phases of the 18.61-year cycle since 1990. The transition from open mangrove woodland and open forest to closed mangrove forest occurred across one-quarter (~500 km^2) of the maximum closed forest area (~1900 km^2). In the Arnhem bioregion, the 2015–2016 El Niño was timed at the tidal amplitude maximum within the 18.61-year cycle, the period of the nodal tidal cycle during which mangrove forests are expected to be least prone to canopy

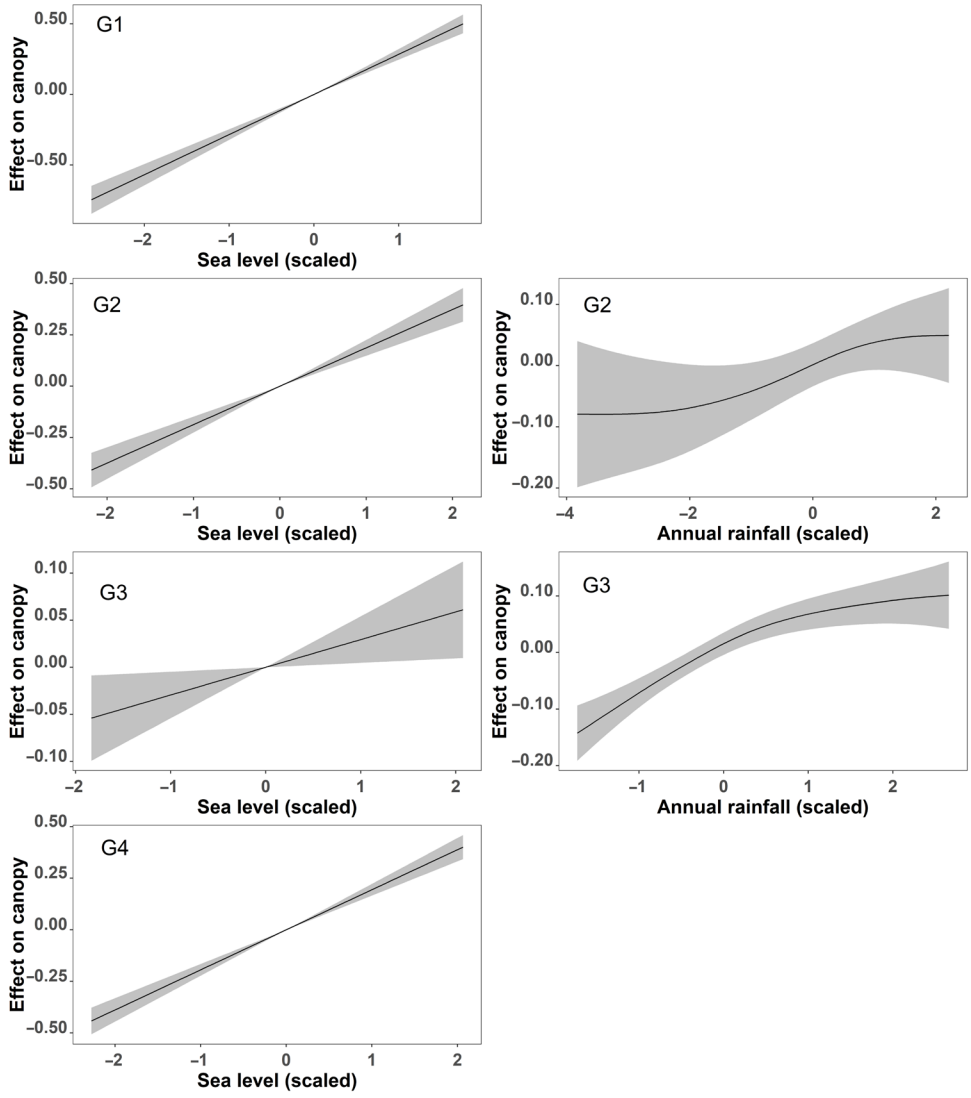

Fig. 4. The response of mangrove canopy cover to lowest maximum monthly sea level and rainfall in the four bioregion groupings. Note that rainfall was not included in the final model for G1 and G4 (table S1).

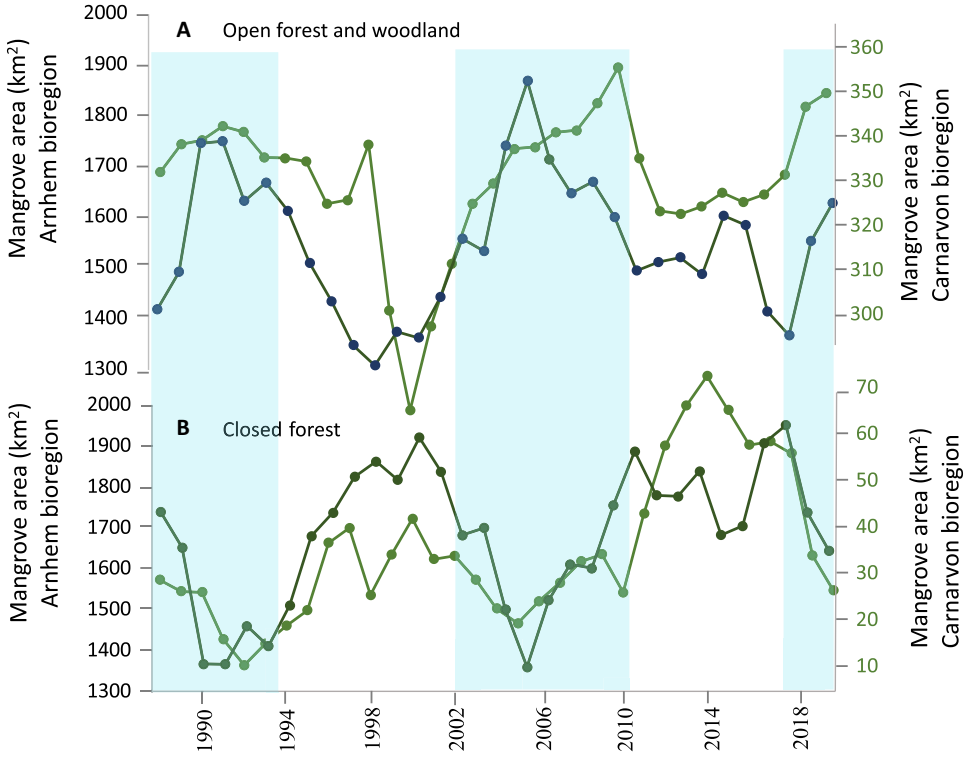

Fig. 5. Canopy tracking the nodal cycle in the G2 (semidiurnal/nodal cycle) bioregions. The area of open forest and woodland (**A**) and closed forest (**B**) in the Arnhem bioregion (dark green) and Carnarvon bioregion (light green) (two-year running means). The trend follows two phases of the 18.61-year nodal cycle (see also Fig. 4), with alternating phases of closed and open canopy associated with a positive anomaly (no shading) or negative anomaly (blue shading), in tide range respectively.

dieback. While the trend toward higher closed forest cover is reversed in 2015–2016, this was quickly restored, suggesting resilient responses of mangroves in this bioregion and limited mortality (Fig. 5).

Within the Gulf of Carpentaria, the maximum sea level exerts the strongest control over mangrove canopy of all bioregions ($P < 0.001$) (Fig. 4), and inclusion of monthly tidal SD (an indicator of the nodal tidal cycle) explains 90% of variation in mangrove canopy cover (table S2). Here, tides are diurnal, with the result that the phase of the 18.61-year nodal tidal cycle is the inverse of the neighboring Arnhem bioregion (Figs. 2 adn 6D). The minimum amplitude of the 18.61-year nodal tidal cycle occurred in 2015, coincident with the minimum amplitude of the 4.4-year perigean harmonic (Fig. 6, C and D), a combination with a return period of ~40 years. The resulting extreme moderation of tidal amplitude in that year (~0.45 m lower than the maxima; Fig. 6C) explains most of the observed decline in maximum tide level over the period 2007–2015. The coincident strong El Niño lowered mean water level and extended the dry season, which normally occurs between May and October, into November (*11*). A phase of canopy dieback that had commenced in the Gulf of Carpentaria in 2012 (Fig. 6) was exacerbated by drought, resulting in more extensive mangrove mortality and sustained canopy loss than occurred in the adjacent Arnhem bioregion, where we propose that the impact of the El Niño was tempered by the high amplitude phase of the nodal tidal cycle.

We hypothesized that mangrove canopy cover would be influenced by changes in maximum tidal range at the 4.4-year perigean cycle in the northern Great Barrier Reef, Kimberly, Bonaparte, and Dampier bioregions, where this cycle predominates (Fig. 1). Spring tides are lowest in the late dry season (August to October), at the time of lowest rainfall and maximum water stress. Years in which these tides are particularly low are phased with the 4.4-year subharmonic and are associated with lower closed forest cover ($P = 0.636$, $P = 0.682$, $P = 0.274$, and $P = 0.686$ for the Dampier, the northern Great Barrier Reef, Bonaparte, and Kimberly bioregions, respectively; Fig. 7 and Materials and Methods). However, annual rainfall had a stronger predictive influence on canopy cover in these bioregions than maximum dry season tide level, with the additive term of rainfall explaining 96.5% of the deviance with adjusted $r^2 = 0.96$ (table S2). Rainfall also dominated the interannual variability in group 4, the southeastern bioregions of Southern Queensland, South East Coast, and Temperate Southern Coast, a finding consistent with previous assessments (*15*, *16*), and the relatively low amplitude of long phase tidal harmonics in the region (4 to 6 cm).

Patterns of mangrove loss and expansion in the Norman River in the eastern corner and the Roper River in the western corner of the Gulf of Carpentaria (Fig. 8) illustrate the importance of geomorphic context in the expansion and contraction of mangrove canopy cover. In both estuaries, mangrove expansion continues at the tidal head in 2014–2016, while dieback is concentrated in geomorphic settings subject to the full tidal range (mudflats fringing coastlines and river channels) (*19*).

DISCUSSION

The trend of mangrove proliferation and thickening has been noted for mangrove poleward limits globally (*20*) and, in Australia, is

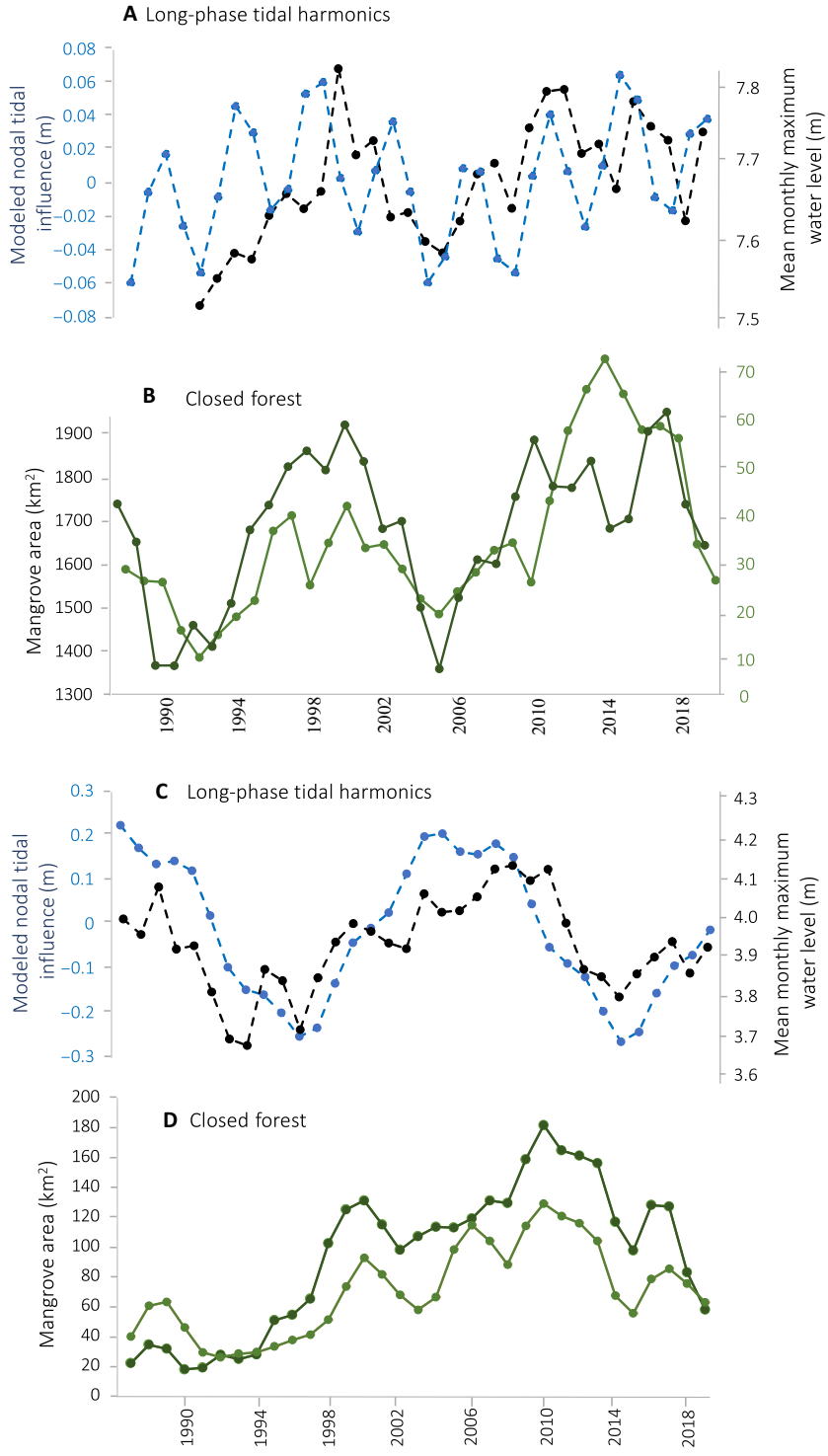

Fig. 6. The 18.6-year lunar nodal cycle in relation to mangrove canopy cover. Modeled combined influence of the 18.6 nodal tidal cycle and 4.4-year perigean subharmonic on the 99.5 percentile tide (combined; blue dashed lines) and observed average monthly maximum water level (black dashed lines) in Milner Bay, Arnhem Bioregion (**A**), and Karumba in the corner subregion of the Gulf of Carpentaria (**C**), illustrating the 180° shift in phasing of the 18.61-year cycle. The 2-year running mean area of mangrove closed forest (**B**) within the Arnhem bioregion (dark green) and the Carnarvon bioregion (light green) and the 2-year running mean area of mangrove closed forest (**D**) within the northern territory (dark green) and the corner (light green) subregions of the Gulf of Carpentaria (locations in Fig. 1). An intense El Niño in 2015–2016 is coincident with the maxima of tidal amplitude in Arnhem Land and the minima of tidal amplitude in the Gulf of Carpentaria.

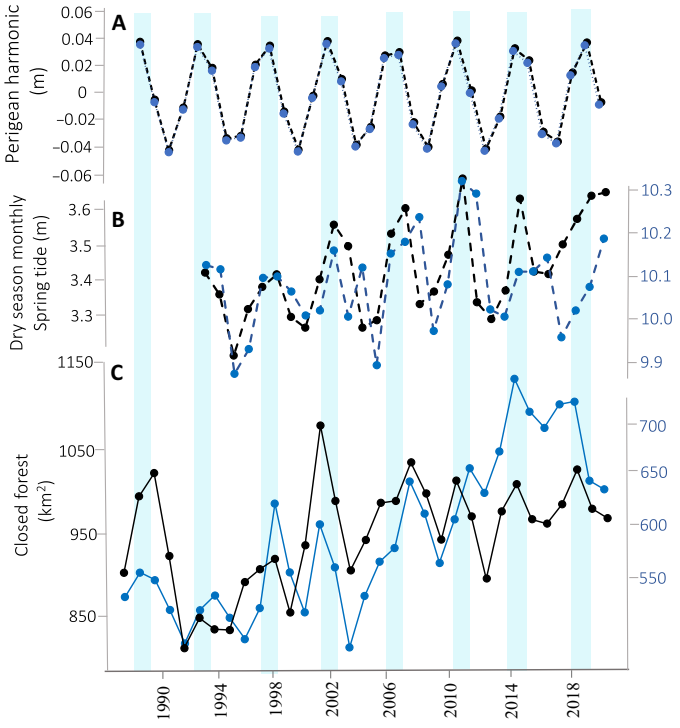

Fig. 7. The perigean subharmonic in relation to spring tidal level and mangrove canopy on opposite sides of the northern Australian continent. The modeled influence of the Perigean subharmonic (**A**) at Broome, Western Australia (black dashed line) and Cape Fergusson, Queensland (blue dashed line); mean monthly maximum water level for the late dry season (August to October) (**B**) at Broome tidal gauge, Western Australia (black dashed line) and Cape Ferguson, Queensland (blue dashed line). Area of closed canopy mangrove forest (2-year running means) in the Kimberly and Dampier bioregions (combined; black solid line) and the northern Great Barrier Reef (blue solid line) (**C**). The eight periods' positive anomaly/high tidal amplitude (blue shading) aligns with phases of higher mangrove canopy cover, but rainfall is a stronger predictor of interannual variability.

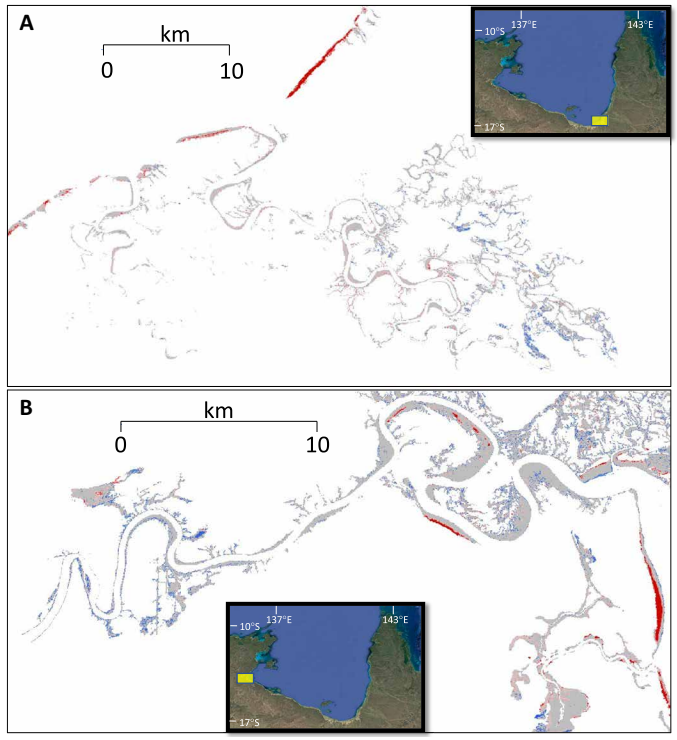

Fig. 8. Geomorphic context of mangrove dieback in the Gulf of Carpentaria. Patterns of mangrove expansion (blue) and dieback (red), no change (gray) between 2014 and 2016 in the Norman River at Karumba (17°28′S; 140°48′E) (**A**) and the Roper River (14°42′S; 135°17′E) (**B**), Gulf of Carpentaria. Dieback is concentrated in areas of full tidal range, while expansion continues at the tidal head, where tidal range is dampened.

ubiquitous across latitudes and bioregions in this study. Mangrove expansion is consistent with moderate rates of sea level rise (Table 1) and other global drivers favoring mangrove growth, including elevated atmospheric CO_2 and, in higher latitudes, temperature (*20*, *21*). We propose that long-phase tidal modulation is an important control over mangrove canopy condition in Australia. While the long-phase tidal components modify tidal amplitude by about 3% (*3*), in macrotidal regions, this component can translate into 20 to 50 cm of interannual variability in high water levels (*7*). Because mangroves occupy gently sloping upper intertidal mudflats, the 18.61- and 4.4-year modulations have influenced interannual variation in controlling mangrove canopy cover hydroperiod and mangrove growth.

We provide three lines of evidence supporting a role for the lunar nodal cycle. First, the alternation between open and closed canopy in semidiurnal coastlines follows the negative and positive phasing of the 18.6-year nodal cycle, a phasing discernible across all bioregions (Fig. 3) and particularly dominant in regions where the nodal cycle influence is pronounced (the Arnhem, Carnarvon, and Gulf of Carpentaria bioregions; Fig. 4). Observations from the 2015 dieback event suggest that the gray mangrove *Avicennia marina* is particularly susceptible to canopy decline under reduced inundation (*11*). *A. marina* is the most widely distributed species in Australia, dominating subtropical and temperate mangroves, and this may explain the consistency of the nodal cycle influence on mangrove canopy cover across the continent.

Second, the alternate phasing of the nodal cycle in the diurnal coastline of the Gulf of Carpentaria is associated with a corresponding shift in the phasing of canopy cover, with the maintenance of high canopy cover with the 2006 optima and stronger declines associated with the 2015 minima. While there is little doubt that the strong El Niño event contributed to mangrove mortality, we propose that the coincidence of the El Niño with the minimum tidal amplitude phase of the nodal cycle in the Gulf of Carpentaria was the reason for much higher mortality in this bioregion than in adjacent semidiurnal bioregions where the El Niño coincided with the high amplitude phase.

Third, the pattern of dieback within estuaries during the 2015–2016 event in the Gulf of Carpentaria suggests declines to be concentrated in areas subject to full tidal amplitude (and therefore tidal range dampening during the nodal cycle minima). Within the Roper and Norman Rivers, mangrove expansion continues through the El Niño drought of 2015–2016, where tidal range and the influence of the tidal modulation are limited, but the effects of sea level rise remain. This expansion occurs despite these environments consisting of newly recruited trees subject to the full effect of low rainfall, reduced freshwater inflow, and higher temperature observed at the time (*11*).

The impact on mangrove ecosystem processes associated with these nodal cycle events is likely to be profound. In the Arnhem bioregion, the 18.61-year nodal cycle drove the transition between

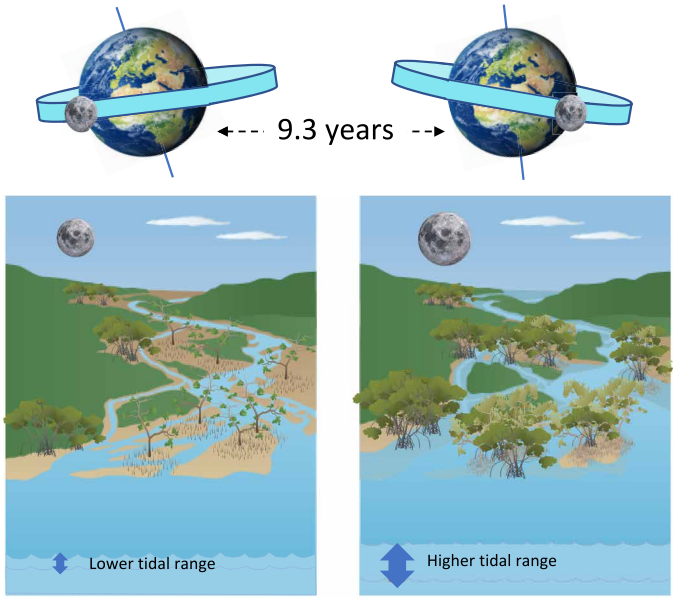

Fig. 9. Conceptual model of the influence of the nodal cycle on mangrove canopy cover. The precession of the lunar nodes has an influence on tidal amplitude, and this influence on inundation high in the tidal frame may be relatively large over the 18.61-year cycle compared to climatic drivers. The vigor of mangrove growth may reflect this periodicity, thereby influencing canopy cover, litterfall, and carbon burial rates.

open and closed canopy cover for 25% of the mangrove forest areal extent, some 500 km^2 of forest. In the Gulf of Carpentaria, where the coincident minima of the 18.61- and 4.4-year modulations in 2015 occurred during intense El Niño event, the proportion of closed mangrove canopy subject to dieback was ~50%. The coincidence between recent intense El Niño and troughs of the 18.61-year cycle (1997–1998 and 2014–2015) has been previously noted (*22*, *23*), and on these occasions, mangroves in diurnal settings subject to full tidal range are particularly vulnerable to loss (*24*).

Tide gauge analyses suggest that an influence of the 18.61-year nodal cycle comparable to that observed in our study (>10-cm range) is evident in Central America, Vietnam, Thailand, the Philippines, and Indonesia (*7*). Together with Australia, these regions contain 55% of the world's remaining mangroves (*25*). Given the disproportionately important role tropical mangroves play as a natural carbon sink (*26*), variability in canopy cover at regional and global scales would influence the rate of atmospheric carbon drawdown over decadal time scales. Canopy extent maxima might be expected in ~2024 in Indochina, Borneo, and the Philippines and in ~2033 in Indonesia and Central America, on the basis of phases in nodal modulation (*7*).

MATERIALS AND METHODS

Conceptual model and analytical approach

The position within the tidal frame suitable for mangrove colonization may vary with hydrological, geomorphological, and edaphic conditions, but in general, Australian mangroves are situated between mean high water and mean high water spring tidal levels, with the extent of cover of mangrove at upper intertidal positions dependent on aridity conditions (*27*, *28*). Mangroves are therefore more likely influenced by alterations to the periodicity of high water levels than mean or low water levels within the tidal frame. Changes to the frequency and duration of high-tide inundation caused by lunar precession is likely to be expressed in alterations to soil water content and soil water salinity. We hypothesize that these effects will be most pronounced during the dry season in tropical climates, when spring tide inundation is lower than at other times due to prevailing easterly trade winds (*18*), and mangroves most susceptible to water stress. The immediate response to water stress is expected to be canopy thinning (Fig. 9). While mangrove extent may also be influenced by changes to hydroperiod in the upper intertidal, the timing and observation of these changes are likely to be lagged in relation to this driver and more influenced by changes to mean sea level at the tidal head. We therefore focused on the response of mangrove canopy cover to maximum water level changes driven by long-period tidal cycles, along with other putative drivers such as rainfall.

Our approach was to use a prior classification of Australian coastal bioregions (*29*) as a framework for comparing the influence of tidal cycles on mangrove canopy cover at a continental scale (Fig. 1). We matched bioregions with the modeled influence of the 18.61-year nodal cycle and the 4.4-year perigean subharmonic, which vary predictably across the continent in relation to coastal morphology, tidal range, and tidal form factor (the extent of diurnal versus semidiurnal tidal form). The timing of the 18.61-year lunar nodal cycle varies between diurnal and semidiurnal settings (*1*), with the maximum amplitude in semidiurnal settings corresponding to the minimum amplitude in diurnal settings. This allowed for testing of the influence of the nodal cycle along coastlines subject to common climatic influence but contrasting tidal form. Because the Gulf of Carpentaria was the only region with a diurnal tide subject to the 18.6-year nodal cycle, the region was subdivided to improve replication (Northern Territory and Corner and Peninsula subregions; Fig. 1).

Mangrove extent and canopy cover

Mangrove extent and canopy cover was defined using methods described by Lymburner *et al.* (*14*). Limits of mangrove extent used to constrain the analysis were defined using the global trend and extent maps generated by the Global Mangrove Watch, which used both Landsat time series and Advanced Land Observation Satellite (ALOS) Phase Array L-band Synthetic Aperture Radar data from a baseline year of 2010, with subsequent annual change away from this baseline from 1996 to 2016 (*30*). Available Landsat 5 Thematic Mapper, Landsat 7 Enhanced Thematic Mapper Plus, and Landsat 8 Operational Land Imager observations have been geometrically corrected, converted to surface reflectance, adjusted for solar illumination and viewing angles, restructured to remove cloud and cloud shadow, and archived within the National Computational Infrastructure Facility at the Australian National University from 1987 onward. For each year between 1987 and 2020, the 10th percentile green photosynthetic fraction (GV_{10}) was calculated, identifying vegetated areas persistently green throughout the year (mangroves as opposed to sympatric herbaceous and woody vegetation). PCC% was determined at selected locations using light detection and ranging–derived canopy height models with a resolution of ~≤1 m. GV_{10} was subsequently related to PCC% using 50% of the PCC% dataset, while the remaining PCC% dataset was used for validation. Following validation, GV_{10} was calibrated against PCC% for each year to indicate spatial and temporal changes in mangrove canopy cover (*14*).

Environmental variables

Monthly maximum, mean, and minimum water levels were accessed using tide gauge records from the Australian Baseline Sea Level Monitoring Project, managed by the Australian Bureau of Meteorology (www.bom.gov.au/oceanography/projects/abslmp/abslmp.shtml). Stations within this network provide reasonable coverage of the marine and coastal bioregions, as follows: Gulf of Carpentaria: Milner Bay/Groote Eylandt tide gauge (13.8600°S, 136.4158°E), Karumba storm tide gauge (17.50°S, 140.8333°E), and Weipa tide gauge (12.6666°S, 141.8666°E); Kakadu: Darwin Harbour tide gauge (12.4719°S, 130.8458°E); Dampier and Kimberly bioregions: Broome tide gauge (18.0008°S, 122.2183°E); Carnarvon bioregion: Hillarys tide gauge (31.8256°S, 115.7286°E); Northern Great Barrier Reef bioregion: Cape Ferguson tide gauge (19.2774S, 147.0586°E); Southern Great Barrier Reef: Rosslyn Bay tide gauge (23.1610°S, 150.7901°E); Southeast Coast: Port Kembla tide gauge (34.4734°S, 150.9118°E); and Temperate Southern Coast: Portland tide gauge (38.3439°S, 141.6136°E). Data gaps were filled by spline interpolation if the number of consecutive missing data points is less than 4. However, if more data are missing, then regression with records from nearby stations was used. In addition, the monthly Southern Oscillation Index (SOI) for the study period was downloaded from National Oceanic and Atmospheric Administration (NOAA)'s Climate Prediction Center (www.cpc.ncep.noaa.gov/data/indices/soi).

Monthly rainfall aggregate and mean maximum temperature were accessed from the Australian Bureau of Meteorology, Climate Data Online (www.bom.gov.au/climate/data). Stations were chosen for continuity of record over the analysis period: Gulf of Carpentaria (Centre Island, Karumba, and Weipa), the Carnarvon Bioregion (Exmouth), Northern Great Barrier Reef (Cairns), Southern Great Barrier Reef (Mackay), SE Queensland (Hervey Bay), South East Coast (Williamstown air base), Arnhem bioregion (Darwin), Bonaparte bioregion (Darwin), Kimberley bioregion (Broome). Dampier bioregion (Broome), and Temperate Southern Coast (Melbourne).

Modeling of long-phase tidal cycle influence

To extract the magnitude and phase of the 18.61-year lunar nodal tidal cycle and the 8.85-year cycle of lunar perigee at sites around the coastline of Australia, we followed (*1*). We used tidal constituents from the TPXO7.2 global tidal model from Oregon State University. Using these constituents (which have a one-quarter degree resolution), we predicted multidecadal time series of astronomical tides at different sites around the coast of Australia using the Tidal Model Driver (TMD) MATLAB toolbox created by scientists at Earth & Space Research. TMD includes standard satellite modulation corrections based on equilibrium tide expectations. From the time series of predicted tidal series, we extracted annual time series of the 99th percentile. The amplitude and phase of the tidal modulations and their subharmonics were estimated from the annual percentile time series using harmonic analysis fitted to 18.61-, 9.305-, 8.85-, and 4.4-year sinusoidal signals. The amplitudes of the 9.305- and 8.85-year cycles were typically more than an order of magnitude smaller than that of the 18.61- and 4.4-year cycles, respectively, and, hence, were not considered further.

To test the influence of the nodal cycle and perigean subharmonic on mangrove canopy cover, we first assessed the relationship between modeled maximum tide and observed maximum tide for representative tide stations (listed above) and, second, the relationship between observed lowest maximum tide (the dry season maximum tides in the tropics) and mangrove canopy cover (as described below).

Statistical modeling of mangrove extent and canopy cover

A two-step modeling approach was used to explore the dynamics of mangrove extent (i.e., total mangrove area in a coast bioregion) and canopy conditions (i.e., the proportion of closed forest). Generalized additive mixed models (*31*) were used to decompose the time series of mangrove area and condition into (i) a global length-of-record trend component and (ii) a component for short-term fluctuations within coastal bioregions (*32*, *33*). GAMM is a semiparametric extension of generalized linear models, which can account for the nonlinear relationships between dependent variables and covariates (*34*, *35*). A GAMM was applied to each coastal bioregion to investigate the response of mangroves to tidal and climatic variables described above. First, we used GAMM (*34*) to decompose the time series of mangrove area and canopy cover into a global long-term trend component and a component for short-term fluctuations within each coast bioregion (*32*, *33*). Second, we investigated the response of mangrove to environmental variations (i.e., sea level and rainfall) by fitting individual GAMM for every coastal bioregion. To make it easier to interpret the estimated coefficients, all environmental variables for a site were standardized before model building such that each observation was subtracted from the mean and divided by the SD. The resulting scaled data had a mean of 0 and an SD of 1, providing internal consistency and facilitating comparison between environmental variables and among bioregions. The total mangrove area was also standardized within each bioregion to allow the comparisons between sites so that observed changes were analyzed at the same scale. We followed (*36*) for variable selection by adding an additional penalty term in the smoothness selection procedure, thereby removing redundant covariates.

As the variable of mangrove canopy condition is a proportion (calculated as the ratio of the closed forest and the total mangrove area, and ranging from 0 to 1 may not be normally distributed), we tested three error distribution families—Beta, Gamma, and Gaussian—for model fitting, with the result that Beta was chosen as the link function for GAMM. We also checked the autocorrelation in model residuals using the Durbin-Watson test (*37*).

To explore how sea level influences mangrove dynamics, we considered three sea level variables: mean meanly sea level, the lowest maximum monthly sea level, and the SD of monthly sea level. To examine the possible lagged mangrove response to environmental forcing, we considered lags of up to 3 years but all lagged environmental variables statistically insignificant ($p < 0.05$). Each model was fitted with annual total rainfall, mean SOI, and one of the sea level variables. Variable selection was based on the chi-square test (*35*). However, in cases of nonsignificant chi-square test ($P > 0.05$), the model with the lowest Akaike information criterion was selected and reported on. In all cases, SOI was not selected, suggesting that this index lacked explanatory power at the bioregional level of study.

The time series of area of closed mangrove forest displayed a monotonic increasing trend in all regions except South East Queensland ($P = 0.65$) and Temperate Southern Coast ($P = 0.21$) based on the Mann-Kendall test (*38*). We tested whether the dynamics of closed forest area were synchronous with the variation in spring high tides using a nonparametric test suitable for testing synchronism of trends in multiple time series (*39*). The modeling procedures were carried out with the "mgcv" package (*35*). Package "funtimes" (*39*) was used for the trend tests. All statistical analyses were carried out using the R v4.1.0 statistical software (*40*).

Elevation of mangroves in the Roper River and Norman River

We illustrate the pattern of mangrove decline and advance within estuaries in the Gulf of Carpentaria in the period 2014–2016 using two representative case studies: the Roper River in the SE corner of the Gulf and the Norman River in the SW corner (Fig. 9). We used the ALOS Global Digital Surface Model, namely, the ALOS World 3D at 30-m spatial resolution (AW3D30) (www.eorc.jaxa.jp/ALOS/en/dataset/aw3d30/aw3d30_e.htm), to generate the elevations of the mangrove dieback (red color; Fig. 3) zone and the mangrove expansion (blue color; Fig. 8) zone in the Norman and the Roper Rivers. First, we downloaded the AW3D30 covering the two rivers and extracted the elevation values for all pixel classes computed from the raster datasets archived in Digital Earth Australia between 2014 and 2016 using Landsat time series data (https://maps.dea.ga.gov.au/#share=s-t59vXkV2NWTL9Hvf2hSB0uqLcAb). We compared the elevations of the mangrove dieback and the mangrove expansion zones to establish whether there was a significant difference in elevation between each zone in each river. The *t* test was used to test the significant difference in elevation between the two zones in each river.

SUPPLEMENTARY MATERIALS

Supplementary material for this article is available at https://science.org/doi/10.1126/sciadv.abo6602

REFERENCES AND NOTES

1. I. D. Haigh, M. Eliot, C. Pattiaratchi, Global influences of the 18.61 year nodal cycle and 8.85 year cycle of lunar perigee on high tidal levels. *J. Geophys. Res. Oceans* **116**, C06025 (2011).
2. A. Oost, H. De Haas, F. Ijnsen, J. M. Van den Boogert, P. L. De Boer, The 18.6 yr nodal cycle and its impact on tidal sedimentation. *Sediment. Geol.* **87**, 1–11 (1993).
3. N. Gratiot, E. J. Anthony, A. Gardel, C. Gaucherel, C. Proisy, J. T. Wells, Significant contribution of the 18.6 year tidal cycle to regional coastal changes. *Nat. Geosci.* **1**, 169–172 (2008).
4. A. Smith, L. Guastella, S. Bundy, A. Mather, Combined marine storm and Saros spring high tide erosion events along the KwaZulu-Natal coast in March 2007: News & views. *S. Afr. J. Sci.* **103**, 274–276 (2007).
5. P. R. Thompson, M. J. Widlansky, B. D. Hamlington, M. A. Merrifield, J. J. Marra, G. T. Mitchum, W. Sweet, Rapid increases and extreme months in projections of United States high-tide flooding. *Nat. Clim. Chang.* **11**, 584–590 (2021).
6. K. McKee, K. Rogers, N. Saintilan, Response of salt marsh and mangrove wetlands to changes in atmospheric CO_2, climate and sea level, in *Global Change and the Function and Distribution of Wetlands* (Springer, 2012), pp. 63–96.
7. D. Peng, E. M. Hill, A. J. Meltzner, A. D. Switzer, Tide gauge records show that the 18.61-year nodal tidal cycle can change high water levels by up to 30 cm. *J. Geophys. Res. Oceans* **124**, 736–749 (2019).
8. A. D. Knighton, C. D. Woodroffe, K. Mills, The evolution of tidal creek networks, Mary river, northern Australia. *Earth Surf. Process. Landf.* **17**, 167–190 (1992).
9. C. Woodroffe, J. Chappell, B. Thom, *Geomorphological Dynamics and Evolution of the South Alligator Tidal River and Plains, Northern Territory* (The Australian National University, North Australia Research Unit, 1986).
10. M. E. Mulrennan, C. Woodroffe, Saltwater intrusion into the coastal plains of the Lower Mary River, Northern Territory, Australia. *J. Environ. Manage.* **54**, 169–188 (1998).
11. N. C. Duke, J. M. Kovacs, A. D. Griffiths, L. Preece, D. J. E. Hill, P. van Oosterzee, J. Mackenzie, H. S. Morning, D. Burrows, Large-scale dieback of mangroves in Australia's Gulf of Carpentaria: A severe ecosystem response, coincidental with an unusually extreme weather event. *Mar. Freshw. Res.* **68**, 1816–1829 (2017).
12. K. J. Allen, D. C. Verdon-Kidd, J. Z. Sippo, P. J. Baker, Compound climate extremes driving recent sub-continental tree mortality in northern Australia have no precedent in recent centuries. *Sci. Rep.* **11**, 18337 (2021).
13. N. Duke, M. Ball, J. Ellison, Factors influencing biodiversity and distributional gradients in mangroves. *Glob. Ecol. Biogeogr. Lett.* **7**, 27–47 (1998).
14. L. Lymburner, P. Bunting, R. Lucas, P. Scarth, I. Alam, C. Phillips, C. Ticehurst, A. Held, Mapping the multi-decadal mangrove dynamics of the Australian coastline. *Remote Sens. Environ.* **238**, 111185 (2020).
15. L. Eslami-Andargoli, P. Dale, N. Sipe, J. Chaseling, Mangrove expansion and rainfall patterns in Moreton Bay, southeast Queensland, Australia. *Estuar. Coast. Shelf Sci.* **85**, 292–298 (2009).
16. A. A. Whitt, R. Coleman, C. E. Lovelock, C. Gillies, D. Ierodiaconou, M. Liyanapathirana, P. I. Macreadie, March of the mangroves: Drivers of encroachment into southern temperate saltmarsh. *Estuar. Coast. Shelf Sci.* **240**, 106776 (2020).
17. L. Eslami-Andargoli, P. Dale, N. Sipe, Does spatial scale affect the pattern of mangrove change under different rainfall regimes? An example in southeast Queensland, Australia. *Austral Ecol.* **38**, 208–218 (2013).
18. A. Forbes, J. Church, Circulation in the Gulf of Carpentaria. II. Residual currents and mean sea level. *Mar. Freshw. Res.* **34**, 11–22 (1983).
19. E. Asbridge, R. Bartolo, C. M. Finlayson, R. M. Lucas, K. Rogers, C. D. Woodroffe, Assessing the distribution and drivers of mangrove dieback in Kakadu National Park, northern Australia. *Estuar. Coast. Shelf Sci.* **228**, 106353 (2019).
20. N. Saintilan, N. C. Wilson, K. Rogers, A. Rajkaran, K. W. Krauss, Mangrove expansion and salt marsh decline at mangrove poleward limits. *Glob. Chang. Biol.* **20**, 147–157 (2014).
21. K. C. Cavanaugh, E. M. Dangremond, C. L. Doughty, A. P. Williams, J. D. Parker, M. A. Hayes, W. Rodriguez, I. C. Feller, Climate-driven regime shifts in a mangrove–salt marsh ecotone over the past 250 years. *Proc. Natl. Acad. Sci.* **116**, 21602–21608 (2019).
22. I. Yasuda, Impact of the astronomical lunar 18.6-yr tidal cycle on El-Niño and Southern Oscillation. *Sci. Rep.* **8**, 15206 (2018).
23. R. S. Cerveny, J. A. Shaffer, The moon and El Niño. *Geophys. Res. Lett.* **28**, 25–28 (2001).
24. S. Abhik, P. Hope, H. H. Hendon, L. B. Hutley, S. Johnson, W. Drosdowsky, J. R. Brown, N. C. Duke, Influence of the 2015–2016 El Niño on the record-breaking mangrove dieback along northern Australia coast. *Sci. Rep.* **11**, 20411 (2021).
25. D. A. Friess, K. Rogers, C. E. Lovelock, K. W. Krauss, S. E. Hamilton, S. Y. Lee, R. Lucas, J. Primavera, A. Rajkaran, S. Shi, The state of the world's mangrove forests: Past, present, and future. *Annu. Rev. Env. Resour.* **44**, 89–115 (2019).
26. T. B. Atwood, R. M. Connolly, H. Almahasheer, P. E. Carnell, C. M. Duarte, C. J. Ewers Lewis, X. Irigoien, J. J. Kelleway, P. S. Lavery, P. I. Macreadie, O. Serrano, C. J. Sanders, I. Santos, A. D. L. Steven, C. E. Lovelock, Global patterns in mangrove soil carbon stocks and losses. *Nat. Clim. Chang.* **7**, 523–528 (2017).
27. B. G. Thom, L. Wright, J. M. Coleman, Mangrove ecology and deltaic-estuarine geomorphology: Cambridge Gulf-ord river, western Australia. *J. Ecol.* , 203–232 (1975).
28. E. Gilman, J. Ellison, R. Coleman, Assessment of mangrove response to projected relative sea-level rise and recent historical reconstruction of shoreline position. *Environ. Monit. Assess.* **124**, 105–130 (2007).
29. R. Thackway, I. D. Cresswell, A bioregional framework for planning the national system of protected areas in Australia. *Nat. Areas J.* **17**, 241–247 (1997).
30. P. Bunting, A. Rosenqvist, R. Lucas, L. M. Rebelo, L. Hilarides, N. Thomas, A. Hardy, T. Itoh, M. Shimada, C. Finlayson, The global mangrove watch—A new 2010 global baseline of mangrove extent. *Remote Sens. (Basel)* **10**, 1669 (2018).
31. T. Hastie, R. Tibshirani, Generalized additive models (with discussion). *Stat. Sci.* **1**, 297–310 (1986).
32. J. Knape, Decomposing trends in Swedish bird populations using generalized additive mixed models. *J. Appl. Ecol.* **53**, 1852–1861 (2016).
33. E. J. Pedersen, D. L. Miller, G. L. Simpson, N. Ross, Hierarchical generalized additive models in ecology: An introduction with mgcv. *PeerJ* **7**, e6876 (2019).
34. A. Guisan, T. C. Edwards Jr., T. Hastie, Generalized linear and generalized additive models in studies of species distributions: Setting the scene. *Ecol. Model.* **157**, 89–100 (2002).
35. S. N. Wood, *Generalized Additive Models: An Introduction with R* (CRC Press, 2017).
36. G. Marra, S. N. Wood, Practical variable selection for generalized additive models. *Comput. Stat. Data Anal.* **55**, 2372–2387 (2011).
37. J. Durbin, G. S. Watson, Testing for serial correlation in least squares regression: I. *Biometrika* **37**, 409–428 (1950).
38. K. Noguchi, Y. R. Gel, C. R. Duguay, Bootstrap-based tests for trends in hydrological time series, with application to ice phenology data. *J. Hydrol.* **410**, 150–161 (2011).
39. V. Lyubchich, Y. R. Gel, A local factor nonparametric test for trend synchronism in multiple time series. *J. Multivar. Anal.* **150**, 91–104 (2016).
40. R. C. Team (R Foundation for Statistical Computing, 2020).

Acknowledgments

Funding: T.D.P. is supported by a Macquarie University Research Fellowship (Grant No. MQRF0001124-2021). Imagery in the conceptual diagram was sourced from the Integration and Application Network, University of Maryland Center for Environmental Science, including artwork by T. Saxby. This research did not receive any specific grant from funding agencies in the public, commercial, or not-for-profit sectors. **Author contributions:** Conceptualization: N.S. and L.L. Data curation: L.L., E.A., T.D.P., and I.D.H. Formal analysis: N.S., L.W., T.D.P., and I.D.H.

Project administration: N.S. Supervision: N.S. Writing—original draft: N.S. Writing—review and editing: N.S., K.R., J.J.K., and R.L. **Competing interests:** The authors declare that they have no competing interests. **Data and materials availability:** All data needed to evaluate the conclusions in the paper are present in the paper and/or the Supplementary Materials.

Submitted 17 February 2022
Accepted 28 July 2022
Published 14 September 2022
10.1126/sciadv.abo6602

ScienceAdvances

The lunar nodal cycle controls mangrove canopy cover on the Australian continent

Neil Saintilan, Leo Lymburner, Li Wen, Ivan D. Haigh, Emma Ai, Jeffrey J. Kelleway, Kerrylee Rogers, Tien Dat Pham, and Richard Lucas

Sci. Adv. **8** (37), eabo6602. DOI: 10.1126/sciadv.abo6602